Secure Near-Field Location Division Multiple Access via Quantum-Classical Learning Workflow

Quan Minh Nguyen, *Graduate Student Member, IEEE,* Bhaskara Narottama, *Member, IEEE,* Minh-Hien T. Nguyen, *Member, IEEE,* Vishal Sharma, *Senior Member, IEEE,* Quang Nhat Le, *Member, IEEE*, and Trung Q. Duong, *Fellow, IEEE*

***Abstract*—This study realizes secure near-field location division multiple access through employing both a variational quantum circuit and a nature-inspired algorithm. With the escalating demands of the sixth generation (6G) and beyond, there is growing interest in using large numbers of antenna elements, making near-field communications more practical Seizing this opportunity, we leverage near-field communications for a distinct multiple access technique, termed location division multiple access (LDMA), which capitalizes on spatial orthogonality to distinguish users by both angle and distance. Nevertheless, relying on beamforming to direct signals to distinct users poses a clear physical-layer security risk: adversaries might eavesdrop on messages intended for legitimate users, prompting the need to optimize beamforming to enhance security while adhering to wireless systems' constraints. To make matters worse, conventional approaches typically entail multiple matrix inversions, and the optimization problem is far from trivial to solve due to its non-convexity and NP-hardness. To this end, our solution leverages variational quantum circuits (VQC), motivated by the potential benefits offered by quantum computing. On top of that, we improve upon the existing VQC workflows by integrating a classical algorithm, particularly, the differential evolution algorithm, thereby reducing quantum computational resource demands while maintaining high exploration efficiency. We further investigate how different quantum circuit depths influence the balance between expressibility and convergence. Simulation results reveal that our proposed scheme consistently outperforms conventional benchmarks in terms of secrecy rates, while simultaneously satisfying quality-of-service (QoS) constraints and power allocation requirements.**

***Index Terms*—Location division multiple access, near-field communications, physical layer security, variational quantum circuits.**

Q. M. Nguyen, B. Narottama, Q. N. Le are with the Faculty of Engineering and Applied Science, Memorial University, St. John's, NL A1B 3X5, Canada (e-mails: {qmnguyen, bnarottama, qnle}@mun.ca).

M.-H. T. Nguyen and V. Sharma are with with the School of Electronics, Electrical Engineering and Computer Science, Queen's University Belfast, Belfast, U.K (e-mails: {h.nguyen, v.sharma}@qub.ac.uk).

T. Q. Duong is with the Faculty of Engineering and Applied Science, Memorial University, St. John's, NL A1C 5S7, Canada, and with the School of Electronics, Electrical Engineering and Computer Science, Queen's University Belfast, BT7 1NN Belfast, U.K. (e-mail: tduong@mun.ca).

This paper has been accepted in part for presentation at International Conference on Quantum Communications, Networking, and Computing (QCNC 2026) April, 2026, Kobe, Japan.

This work was supported in part by the Canada Excellence Research Chair (CERC) Program CERC-2022-00109, in part by the Natural Sciences and Engineering Research Council of Canada (NSERC) Discovery Grant Program RGPIN-2025-04941, and in part by the NSERC CREATE program (Grant number 596205-2025). The work of M.-H. T. Nguyen and V. Sharma is partly funded by the US-Ireland R&D Partnership Programme, supported by Northern Ireland's Department for the Economy (DfE), for the project, MAARS: Multi-Bessel Antenna with Liquid Crystal Reconfiguration for Angle-Range Secure Communication and is partly funded under Horizon Europe Marie Skłodowska-Curie Actions (MSCA) (Grant agreement ID: 101227604), Advanced Network Connectivity using Harmonious Optical and Radio Technologies.

Corresponding author is Trung Q. Duong.

I. Introduction

THE EVOLUTION toward the sixth generation (6G) wireless networks reflects the escalating demand for massive connectivity, ultra-high data rates, and enhanced security in data transmission. In answer to such challenging requirements, technologies such as high-frequency millimeter-wave (mmWave) and terahertz (THz) bands, together with massive multiple-input multiple-output (mMIMO) systems, are being explored to deliver stable, high-capacity, and energy-efficient communication services [1], [2]. However, the use of such high-frequency channels inevitably introduces severe propagation losses, thereby limiting transmission distances and degrading network performance and reliability [3], [4].

Recently, extremely large-scale antenna arrays (ELAAs) have emerged as a promising solution to address these challenges. Capitalizing on the short wavelengths of mmWave and THz frequencies, ELAAs can realize a substantially larger number of antennas within a limited physical layout [5]. This improvement affords a higher beamforming gain, which mitigates propagation loss and extends transmission range, thereby enhancing link reliability in high-frequency wireless systems. Moreover, ELAA extends the near-field region, which becomes increasingly important in future wireless systems [6]. In general, the wireless transmission region can be distinguished into near-field and far-field ranges, divided by the Rayleigh distance. Unlike conventional far-field communication (FFC), where channel characteristics depend primarily on the transmission angle or beamsteering, near-field communication (NFC) exploits both angle and distance to differentiate users, enabling precise beamfocusing and improved spatial resolution [7]. This transition from planar-wavefront in far-field ranges into spherical wavefront in near-field ranges augments spatial resolution in multi-user systems, allowing the transmitter to focus energy on precise location. Furthermore, the spatial resolution of NFC can approach an ideal limit in which the transmitter can accurately focus multiple superimposed signals on distinct user locations, as the number of antennas becomes very large [8]. In addition, while the near-field region can be categorized into reactive and radiating subregions, practical NFC applications typically rely on the radiating near-field subregion, where signals can be focused on intended users, allowing efficient energy propagation [9], [10], [11]. In contrast, evanescent electromagnetic waves dominate the reactive near-field subregion, which is nearer to the transmit antenna array, and their non-propagating nature causes the power to decay rapidly.

While NFC introduces an additional degree of freedom to focus signals on intended users, the broadcast nature of

wireless channels still renders the communication system vulnerable to malicious users in close proximity. Additionally, the rising number of user devices and their increasing demands require the system to both provide reliable performance and maintain security. This has driven growing interests in physical layer security (PLS), which tackles threats, e.g., eavesdropping, using the physical characteristics of the wireless medium [12], [13]. Unlike network-layer security methods, which depends on cryptographic algorithms to encrypt sensitive data points and protect them regardless of the transmission medium, PLS approaches ensure confidentiality by leveraging physical properties such as fading, noise, and spatial variations. To assess PLS, one notable metric is the secrecy rate, which quantifies the difference in data rates between intended users and potential eavesdroppers. A secure system must ensure a positive secrecy rate to protect sensitive data and maintain the desired QoS.

A. Related Studies

PLS approach has been extensively studied in wireless systems, including cellular, Wi-Fi, and 5G communications [14]–[17]. While these studies primarily focus on conventional FFC, spatial division multiple access (SDMA) shall allow parallel data transmission to multiple users located at different angles. However, when multiple users share the same transmission direction, the spatial resolution of FFC degrades due to inter-user interference [9]. To address this limitation of far-field SDMA, NFC may use beamfocusing, leveraging both angular and distance domains to differentiate users, thereby enabling precise signal targeting while mitigating mutual interference. Taking advantage of the extra resources provided in the distance domain, LDMA can utilize beamfocusing with ELAA to allocate a unique beamforming vector for each user [8]. To reduce hardware costs and power demands in fully digital architectures, particularly in multi-user systems, a hybrid beamforming approach is often adopted as well. Such an integration between multiple-access technique and hybrid beamforming improves spectrum efficiency and fosters secure data transmission, especially in large-scale experiencing high user density.

In line with these advancements, several studies have investigated PLS in NFCs. For instance, a two-stage beamformer design was proposed to improve secrecy capacity in a NFC system with a single legitimate user and an eavesdropper [18]. Nonetheless, the scalability of such a configuration warrants further investigation, as multi-user systems generally impacted by co-channel interference. In addition, the resolution characteristics of non-orthogonal multiple access (NOMA) users and eavesdroppers within NFC systems at different angles and distances were analyzed in [19], highlighting the importance of investigating NFC security. Accordingly, many studies have examined the maximization of NFC security indicators. For example, a semi-definite relaxation (SDR) technique and a successive convex approximation (SCA) algorithm were proposed to maximize the secrecy performance of a NOMA-assisted integrated sensing and communication (ISAC) system [20] . Nevertheless, as the number of users increases, NOMA incurs higher receiver complexity and a pronounced susceptibility to error propagation. Beyond multiple-access techniques, an iterative, manifold-based optimization was employed to approximate the security of hybrid beamforming towards fully-digital performance in [21]. Although this indirect design enhances the overall secrecy rate, it restricts the hybrid beamforming architecture from fully exploring its feasible design space, potentially limiting system performance. Another strategy involves learning-based models to mitigate information leakage [22]. While existing NFC-PLS studies utilize optimization and multiple-access techniques to enhance PLS, they generally overlook the potential of LDMA. Given LDMA's flexibility in spatial resolution and its support for dense user environments, it represents a promising candidate for enhancing NFC security. Yet, this aspect remains largely unexplored.

To fully exploit LDMA's capabilities, advanced learning strategies are needed to efficiently optimize the high-dimensional hybrid beamforming problem inherent in dense NFC architecture. In this context, quantum-based learning has recently emerged as a promising solution due to its broad applicability and potential for exponential speedup. In particular, the collaborative use of quantum and classical learning models in knowledge distillation, where quantum models leverage trained classical models to facilitate training convergence, was demonstrated in [23]. Likewise, quantum learning models can be integrated into federated learning workflows, wherein a centralized quantum model iteratively aggregates the gradients or parameters from quantum models trained locally [24]. Studies have also demonstrated the utility of quantum models for heterogeneous network elements. In [25], a dynamic quantum federated learning was used to enhance the collaborative learning among multiple uncrewed aerial vehicles (UAVs). Despite the potential of quantum-based learning approaches to accelerate convergence and handle high-dimensional problems [26], their exploration within NFC-PLS is still in early stages. Moreover, practical implementation is constrained by current hardware limitations and circuit noise, affecting the scalability of purely quantum solutions, especially in multi-user scenarios. In the present noisy intermediate-scale quantum (NISQ) stage, where platforms can process only limited numbers of qubits [27], quantum-based learning can benefit from operating alongside classical algorithms when addressing taxing tasks such as the high-dimensional beamforming challenges posed by ELAA.

Accordingly, designing hybrid learning workflows that effectively combine the strengths of classical algorithms with quantum-based learning models becomes crucial. For instance, a quantum-classical search algorithm was proposed to search over all possible codeword combinations simultaneously for optimal channel quantization, enabling energy-efficient and low-complexity reconfigurable intelligent surfaces (RIS)-assisted data transmission [28]. The presence of RIS significantly changes the eavesdropping landscape, yet their framework neither models adversarial RIS links nor protects sensitive medical data from interception, leaving PLS completely unaddressed. Existing deep learning-based beamforming methods rely on extensive offline training and large

datasets to approximate optimal beamforming policies [29], [30]. While these approaches can achieve favorable performance, they often suffer from high training complexity and sensitivity to variance of channel conditions [30], [31], [32]. In [33], VQC was incorporated as a layer to enhance the classical neural network in optimizing the beamforming design, thereby improving the network's total data rate. Specifically, the VQC was employed to extract and exploit useful features from the channel state dataset, while its potential to independently achieve optimal solutions was overlooked. Moreover, the approach focuses exclusively on fully digital beamforming, which is energy-inefficient in large-scale multi-user wireless systems. By relying on SDMA rather than LDMA, the method diminishes the immunity of user information against potential adversarial decoding.

Motivated by this gap, we propose a sequential quantum-classical (SQC) algorithm to optimize hybrid beamforming architecture, thereby enhancing secrecy rate in LDMA-NFC systems, as shown in Fig. 1.

B. Contributions and Organization

The following articulates the key contributions of this paper.

- This pioneering study employs VQCs to optimize near-field LDMA. While prior studies such as [34] and [35] apply learning-based methods to improve NFC performance, they do not consider LDMA, which is particularly suited for supporting a growing number of users, as it facilitates distinguishing users based on their relative positions to the antenna array and signal angle of departure (AoD) directions. On top of that, this paper supports the scalability of VQC utilization by combining it with a heuristic algorithm. This approach substantially reduces the number of qubits required, and is therefore relevant for NISQ platforms, which typically process limited numbers of qubits.
- Moreover, this is an early attempt to address the security aspect of near-field LDMA, particularly to maximize the total secrecy rate subject to users' QoS constraints under limited power allocation. Most existing studies concerned with the performance of near-field LDMA, such as [8] and [36], typically assume that all mobile terminals within the area are legitimate, thus overlooking realistic security threats such as eavesdropping, making the paper's focus particularly distinctive. On the other hand, while certain studies such as [18] and [22] address the security aspects of near-field communications, they do not investigate LDMA. To this end, this paper optimizes the base station's hybrid beamforming, to degrade the attacker's achieved rate whilst maintaining the QoS of the legitimate users. This optimization problem is significantly challenging, as it involves strongly coupled variables arising from hybrid beamforming, spherical-wave channel characteristics, and non-convex secrecy-rate formulas. The resulting objective domain becomes highly non-linear, making exact convex reformulations or optimal solutions computationally expensive to obtain.
- To support the practical application of the proposed solution, especially give the present-day limitations on logical qubits, this study reduces the qubit requirement by incorporating classical methods, particularly evolutionary algorithms. The proposed scheme reduces quantum resource requirements and improves scalability under NISQ constraints, thus addressing the limitations of existing generic quantum optimization frameworks [37], [38]. Of note, while some studies consider the constraints on the number of qubits [39], [40] or circuit depth [41], most do not apply these approaches to wireless communications.
- This study investigates how varying VQC architectures influence trainability and expressibility. Specifically, two distinct circuit architectures with dynamically parameterized layers are evaluated to assess their effectiveness in enhancing the system's secrecy rate. The results demonstrate that employing a larger number of qubits increases computational capability, significantly improving secrecy rate performance compared to the reduced layout.

The remainder of this paper is arranged as follows. Section II models the near-field LDMA system and formulates the secrecy rate optimization problem. Section III proposes a sequential quantum-classical workflow for enhancing the beamforming architecture. Section IV evaluates the impact of different transmission environments on the performance of the proposed solution, with particular regard to varying quantum circuit depths. Section V summarizes our findings.

Notations: A matrix and a vector are symbolized by a bold uppercase letter $\mathbf{A}$ and a bold lowercase letter $\mathbf{a}$, respectively. For any matrix $\mathbf{A}$, $\mathbf{A}^H$, $\angle\mathbf{A}$, $[\mathbf{A}]_{i,j}$, and $\|\mathbf{A}\|_F$ denote the conjugate transpose, element-wise phase, *(i,j)*-th entry and Frobenius norm of A, respectively. $\|\cdot\|$ denotes the Euclidean norm of a vector and $|\cdot|$ denotes the magnitude of a scalar. $\mathbb{C}$ stands for the set of complex numbers and $\mathbb{E}$ denotes the mathematical expectation. $\mathbf{I}_K$ is $K \times K$ identity matrix. $|\cdot\rangle$ denotes a column vector in Dirac (ket) notation.

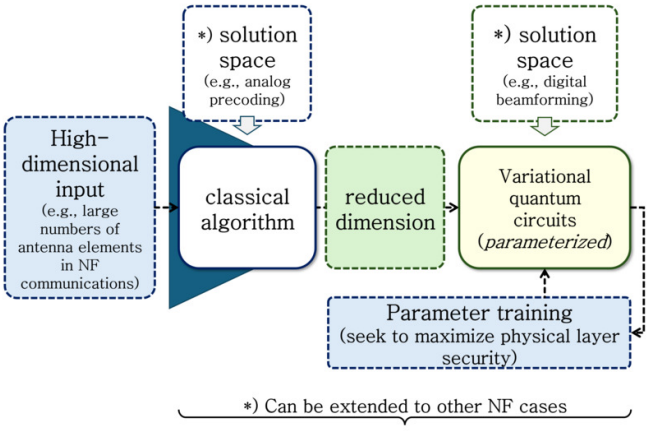

Fig. 1. The core proposition of this paper, which addresses the limitations of current quantum computing, particularly the restricted number of logical qubits. A classical nature-inspired algorithm, particularly a metaheuristic algorithm, is first employed to identify the solution for the analog precoding. Subsequently, variational quantum circuits are employed to find the solution for the digital precoding.

II. System Model and Problem Formulation

In this paper, we consider a downlink multiple-input single-output (MISO) near-field system, where a base station (BS) is equipped with N_T antennas arranged in a uniform linear array (ULA) layout. Each antenna element is indexed by $n \in \{0, 1, \ldots, N_T\}$ where $N_T = 2N+1$. The spacing between antenna elements is given by $d = \frac{\lambda}{2}$, where λ represents the wavelength of transmitted signal. The transmitter simultaneously sends $\mathbf{s} \in \mathbb{C}^{K\times 1}$ signals to K legitimate users in the near-field region that also includes a potential eavesdropper, where $\mathbb{E}\{\mathbf{s}^H\mathbf{s}\} = \mathbf{I}_K$. It is worth noting that the eavesdropper can simply be considered an untrusted user, meaning that the system does not require prior identification of the malicious user. This assumption allows the design of secure transmission strategies that are robust to any user attempting to decode confidential information. Fig. 2 illustrates the near-field ULA-ELAA system. The near-field boundary is determined by the Rayleigh distance, given by $d_R = \frac{2D^2}{\lambda}$ where D is the antenna aperture. As the BS employs ULA for N_T antennas, the antenna aperture is then defined as $D = (N_T-1)d$. Beyond the Rayleigh boundary, the signal propagation transitions into the far-field area, where it exhibits planar wavefront characteristics and the LDMA spatial resolution is no longer preserved. To ensure independent data streams, it is essential that $K \leq N_{RF}$, where N_{RF} is the number of RF chains. For the sake of simplicity, $K = N_{RF}$ is used throughout this paper, following studies such as [8] and [42].

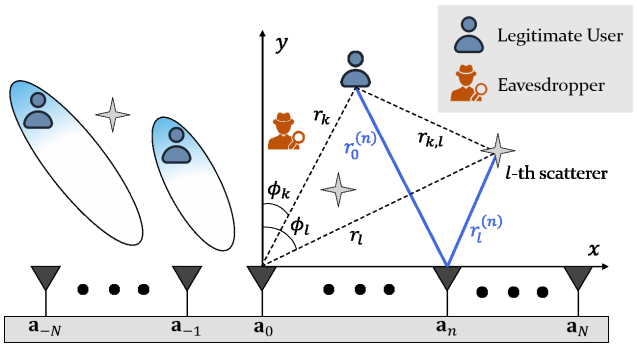

Fig. 2. Near-field ULA-ELAA system under eavesdropping threat.

A. Near-field Channel Model

In a practical scenario, the wireless propagation environment involves L scatterers that introduce non-line-of-sight (NLoS) paths in addition to direct line-of-sight (LoS) transmission. Let $\mathbf{a}_{\delta_n} = [\delta_n d, 0]^T$ be the Cartesian coordinate of the n-th antenna, where $\delta_n = n - N$ denotes the index offset from the central array element. The reference point is set at the center of the array, $\mathbf{a}_0 = [0, 0]$. The positions of the k-th user and the l-th scatterer are, respectively, denoted by $\mathbf{u}_k = [r_k \sin\phi_k, r_k \cos\phi_k]^T$ and $\mathbf{z}_l = [r_l \sin\phi_l, r_l \cos\phi_l]^T$, with ϕ_k and ϕ_l representing the AoD from the BS to the k-th user and l-th scatterer, respectively. Here, r demonstrates the distance between the center of the transmitting array and the user (or scatterer). Hence, the propagation distance between the n-th antenna and the k-th user (or l-th scatterer) can be given by the following expression

$$\begin{aligned} r_l^{(n)} &= \sqrt{r^2 + \delta_n^2 d^2 - 2r\delta_n d \sin\phi} \\ &\approx r - \delta_n d \sin\phi + \frac{\delta_n^2 d^2 \cos^2\phi}{2r}, \end{aligned} \tag{1}$$

where the approximation is obtained by taking the first three terms from the Fresnel approximation [43], with $\sqrt{1+x} \approx 1 + \frac{x}{2} - \frac{x^2}{8}$ for $x = \frac{\delta_n^2 d^2 - 2r\delta_n d\sin\phi}{r^2}$. Specifically, (1) can be represented as follows:

$$r_0^{(n)} = r_k - \delta_n d \sin\phi_k + \frac{\delta_n^2 d^2 \cos^2\phi_k}{2r_k}, \text{for } l = 0 \text{ (LoS)}, \tag{2}$$

$$r_l^{(n)} = r_l - \delta_n d \sin\phi_l + \frac{\delta_n^2 d^2 \cos^2\phi_l}{2r_l}, \forall l \geq 1 \text{ (NLoS)}. \tag{3}$$

The notations $r_0^{(n)}$ and $r_l^{(n)}$ in (2) and (3) respectively denote the distances $d(\mathbf{a}_{\delta_n}, \mathbf{u}_k)$ and $d(\mathbf{a}_{\delta_n}, \mathbf{z}_l)$. According to superposition principle [9], the channel between the transmitter and the k-th user can be described as

$$\mathbf{h}_k = \alpha_0 g_0 \mathbf{b}(r_0^{(n)}, \phi_0) + \frac{1}{\sqrt{L}} \sum_{l=1}^{L} \alpha_l g_l \mathbf{b}(r_l^{(n)}, \phi_l) e^{j\theta_{k,l}}, \tag{4}$$

where $g_0 = \sqrt{\frac{K_{Ri}}{K_{Ri}+1}}$ represents the complex channel gain for the LoS path and K_{Ri} is the Rician fading factor. Meanwhile, $g_l \sim \mathcal{CN}(0, \sigma_{\alpha_l}^2)$ denotes NLoS path gains, each of which is assumed to be independent and identically distributed (i.i.d), with variance $\sigma_{\alpha_l}^2 = \frac{1}{K_{Ri}+1}$. The random phase of the l-th scatterer path to the k-th user follows a uniform distribution, $\theta_{k,l} \sim \mathcal{U}(0, 2\pi)$ [44]. The signal experiences free-space path loss over the two-hop transmission distance $r_l^{(n)}$ and $r_{k,l}$, represented by α_l, where $r_{k,l}$ is the distance between the k-th user and l-th scatterer. In NFC, the spherical wavefronts enable enhanced spatial resolution at a specific location (r, ϕ). ELAA focuses signals on k-th user by employing beamfocusing vectors $\mathbf{b}(r_l^{(n)}, \phi_l)$ from every antenna, which can be expressed as

$$[\mathbf{b}(r_l^{(n)}, \phi_l)]_n = e^{-j\frac{2\pi}{\lambda}\left(-\delta_n d\sin\phi + \frac{\delta_n^2 d^2 \cos^2\phi}{2r}\right)}. \tag{5}$$

As the number of antennas increases, the unit-norm beamfocusing vectors to two different locations with different distances and angles become asymptotically orthogonal under the increasing limit of aperture, i.e., $N_T \to +\infty$, as follows [8]:

$$\lim_{N_T\to+\infty} |\mathbf{b}^H(r_a, \phi_a)\mathbf{b}(r_b, \phi_b)| = 0, \quad \text{for } r_a \neq r_b \text{ and } \phi_a \neq \phi_b. \tag{6}$$

This lays the ground for LDMA which distinguishes the users through both spatial and angular domains, reducing inter-user interference. Unlike conventional FFC, NFC provides precise beamfocusing even for users share the same signal directions with respect to the BS, i.e., $\phi_a = \phi_b$, given by

$$\lim_{N_T\to+\infty} |\mathbf{b}^H(r_a, \phi_a)\mathbf{b}(r_b, \phi_b)| = 0, \text{ for } r_a \neq r_b. \tag{7}$$

B. Hybrid Beamforming Architecture

This paper considers a fully-connected hybrid beamforming technique, where a single radio-frequency (RF) chain controls multiple antennas simultaneously, reducing the reliance on power-hungry RF chains. Specifically, a discrete phase shifter (PS) based-hybrid beamforming architecture with N_{RF} RF chains is employed to transmit the information $\mathbf{s}$ to K users, subject to the practical hardware constraint $N_{RF} \leq N_T$, which ensures that the number of RF chains does not exceed the number of transmit antennas [8], [9]. Initially, a digital beamformer $\mathbf{W}_D \in \mathbb{C}^{N_{RF} \times K}$ processes the original signal in the baseband to direct it towards the intended users while mitigating inter-user interference. Then, each signal s_k is converted to the RF domain via its corresponding RF chain before being processed by the analog beamformer $\mathbf{W}_A \in \mathbb{C}^{N_T \times N_{RF}}$. Phase shifters in the analog beamformer subsequently adjust the phase of each antenna element, precisely directing the signal to the intended users. This mechanism allows independent optimization for the digital and analog beamformer to enhance overall system performance. The respective digital and analog beamforming matrices can be expressed as

$$\mathbf{W}_D = [\mathbf{w}_{D,1}, \mathbf{w}_{D,2}, \ldots, \mathbf{w}_{D,K}], \tag{8a}$$

$$\mathbf{W}_A = [\mathbf{w}_{RF,1}, \mathbf{w}_{RF,2}, \ldots, \mathbf{w}_{RF,N_{RF}}]. \tag{8b}$$

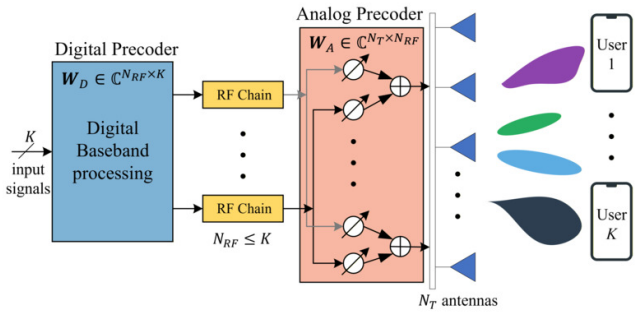

Fig. 3. Fully-connected discrete phase-shifter hybrid beamforming architecture.

Considering the additive white Gaussian noise (AWGN) $\mathbf{n} \sim \mathcal{CN}(0, \sigma^2 \mathbf{I}_K) \in \mathbb{C}^{K \times 1}$, the observed signals at the k-th legitimate user can be given by

$$y_k = \mathbf{h}_k^H \mathbf{W}_A \mathbf{W}_D \mathbf{s} + n_k, \tag{9}$$

where $\mathbf{y} = [y_1, y_2, \ldots, y_K]$. $\mathbf{H}_K = [h_1, h_2, \ldots, h_K]^H \in \mathbb{C}^{K \times N_T}$ describes the channel matrix whose element follows (4). The achievable data rate at k-th user can be written as

$$R_k = \log_2\Big(1 + \frac{|\mathbf{h}_k^H \mathbf{W}_A \mathbf{w}_{D,k}|^2}{\sigma_k^2 + \sum_{m \neq k}^{K} |\mathbf{h}_k^H \mathbf{W}_A \mathbf{w}_{D,m}|^2}\Big). \tag{10}$$

Meanwhile, the eavesdropper intercepts signals from the k-th user at a data rate $R_{e,k}$, determined by

$$R_{e,k} = \log_2\Big(1 + \frac{|\mathbf{h}_e^H \mathbf{W}_A \mathbf{w}_{D,k}|^2}{\sigma_e^2 + \sum_{m \neq k}^{K} |\mathbf{h}_e^H \mathbf{W}_A \mathbf{w}_{D,m}|^2}\Big), \tag{11}$$

where $\mathbf{h}_e \in \mathbb{C}^{N_T \times 1}$ follows (4) considering the location of the e-th eavesdropper, given by $\mathbf{v}_e = [r_e \cos\phi_e, r_e \sin\phi_e]^T$. The secrecy rate quantifies downlink security by measuring the difference between the achievable data rate of a legitimate user, R_k, and that of a potential eavesdropper, $R_{e,k}$. For the k-th legitimate user in the presence of the e-th eavesdropper, it is expressed as

$$\chi_k = [R_k - R_{e,k}]^+, \tag{12}$$

where the term $[\alpha]^+ = \max\{0, \alpha\}$ is used as secrecy rate which cannot be negative [22]. If χ_k becomes zero, the system fails to prevent the e-th eavesdropper from decoding the signal s_k intended for the k-th legitimate user, at a rate equal to or exceeding that of the k-th user.

C. Secrecy Problem Formulation

This paper addresses the joint optimization of the sum secrecy rate across all K legitimate users and power allocation by finetuning the hybrid beamforming architecture, while satisfying the QoS constraint. The optimization problem is formulated as follows:

$$\max_{\mathbf{w}_{D,k}, \mathbf{w}_{RF,j}} \sum_{k=1}^{K} \chi_k \tag{13a}$$

$$\text{s.t. } \chi_k \geq \chi_{min}, \forall k, \tag{13b}$$

$$0 < P \leq P_{max}, \tag{13c}$$

$$|[\mathbf{W}_A]_{j,n}| = 1, \forall j, n, \tag{13d}$$

where $P = \|\mathbf{W}_A \mathbf{W}_D\|_F$ is the total power allocation and the entry $[\mathbf{W}_A]_{j,n}$ corresponds to the j-th RF chain and the n-th antenna element. Constraint (13b) ensures each user's QoS requirement. Constraint (13c) limits the maximum transmitted power of the BS. Since phase shifters only adjust the phase of the signal without affecting its magnitude, constraint (13d) ensures that each analog beamforming vector $[\mathbf{w}_{RF,j}]_n$ has unit-modulus entries with normalized power.

III. Sequential Quantum-Classical Solution

In this section, we propose a sequential hybrid quantum-classical algorithm to optimize the hybrid beamforming architecture. In the first phase, the analog beamformer $\mathbf{W}_A$ is enhanced using a nature-inspired classical optimization technique called differential evolution (DE). DE is a population-based stochastic optimization algorithm that evolves a set of candidate solutions to search for the global optimum. Its effectiveness lies in the balance between the exploration process driven by mutation and crossover operations, and the exploitation towards convergence ensured by the selection phase. The channel state information (CSI) and the digital beamformer, $\mathbf{H}_K$ and $\mathbf{W}_D$, serve as inputs to the DE algorithm, which iteratively determines the optimal analog beamformer $\mathbf{W}_A$ through evolutionary operations. The optimal analog beamformer $\mathbf{W}_A$, along with the channel state information $\mathbf{H}_K$, is then provided as inputs to a variational quantum optimizer (VQO). This enables faster convergence of the VQO, leading to a high-performance design of the digital beamformer $\mathbf{W}_D$. At the end of each iteration, the updated digital beamformer $\mathbf{W}_D$ is fed back into the DE algorithm. The detailed steps of the proposed algorithm are

described in Algorithm 1. To acquire CSI, the transmitter sends a sequence of known pilot signals that the receiver uses to probe the channel. By characterizing the transformation of these pilots through the spherical-wave channel, the receiver reconstructs the full channel matrix. The estimated CSI is then stored as classical data at the network's processing unit and subsequently sampled for use as input to Algorithm 1. In the algorithm, $\mathbf{W}_A^{[t]}$ and $\mathbf{W}_D^{[t]}$ indicate the versions of $\mathbf{W}_A$ and $\mathbf{W}_D$ pertaining to the t-th discrete time unit, $\forall t$.

Algorithm 1 The Integrated Solution.

Input: The acquired channel information $\{\hat{\mathbf{H}}^{[k]}\}_{k=1}^{K}$.
Output: The hybrid beamforming solution $\mathbf{W}_A, \mathbf{W}_D$ and maximum secrecy rate $\chi = \sum_{k=1}^{K} \chi_k$.
1: Define the initial beamforming matrices $\mathbf{W}_A^{[0]}, \mathbf{W}_D^{[0]}$.
2: **for** $t \in t_{max}$ **do**
3: Update $\mathbf{W}_A^{[t]}$ using DE.
4: Update $\mathbf{W}_D^{[t]}$ using VQO.
5: **end for**

A. DE-based Analog Beamformer Design

In this section, we employ DE to jointly optimize the design of the analog beamformer and power allocation, while keeping the digital beamformer $\mathbf{W}_D$ fixed. The employment of ELAA leads to a high-dimensional analog beamforming design problem, which can be effectively addressed by the DE algorithm due to its strong global search capability. The algorithm iteratively generates new candidate solutions from the current population through element-wise scaled difference between randomly selected individuals. This enables effective exploration of the search space. Then, a crossover operation mixes the generated candidates with the population's individuals to introduce diversity, followed by a deterministic selection mechanism that ensures the preservation of superior candidate solutions.

Initialization: The DE algorithm begins by generating multiple analog beamforming matrices, each treated as an individual within the population. To promote convergence toward the feasible region that satisfies constraints (13b)–(13d), it is common to initialize the population using only feasible individuals. Particularly, an initial population $\mathcal{P}^{[0]}$ consisting of M feasible individuals $\mathbf{W}_{A,id} \in \mathcal{P}^{[0]} = \{\mathbf{W}_{A,1}, \ldots, \mathbf{W}_{A,M}\}$ is generated. To ensure that the constraint (13d) is met, we set $\mathbf{W}_A^{[0]} \in \mathbb{C}^{N_T \times N_{RF}}$, where $[\mathbf{W}_A]_{n,j}^{[0]} = \exp(i2\pi\tilde{x}_{n,j}^{[0]})$.

Mutation: In each generation τ, mutant matrices $\mathbf{V}_A^{[\tau]}$, each of which represents a newly generated candidate individual, are built upon the current population of individuals as

$$\mathbf{V}_{A,id}^{[\tau]} = \angle\{\mathbf{W}_{A,best}^{[\tau]} + \zeta \times (\mathbf{W}_{A,r1}^{[\tau]} - \mathbf{W}_{A,r2}^{[\tau]})\}, \tag{14}$$

where ζ is the differential weight factor that controls the mutation variance. $\mathbf{W}_{A,r1}^{[\tau]}$ and $\mathbf{W}_{A,r2}^{[\tau]}$ are randomly chosen from the population $\mathcal{P}^{[\tau]}$, and $\mathbf{W}_{A,best}^{[\tau]}$ is the optimal solution in terms of the fitness function $\mathcal{F}$, described as

$$\begin{aligned}&\mathcal{F}(\mathbf{W}_{A,id})\\ &= \underbrace{\underbrace{-\sum_{k=1}^{K}\chi_k}_{f(\mathbf{W}_{A,id})} + \Big(\epsilon_{DE,1}\sum_{k=1}^{K}\omega(\chi_k) + \epsilon_{DE,2}\rho(P_{id})\Big)}_{F(\mathbf{W}_{A,id})}\\ &+ \eta(\mathbf{W}_{A,id}),\end{aligned} \tag{15}$$

where the first term motivates the improvements of the secrecy rate defined in (13a), and the second term imposes the penalty when the constraints of (13b) and (13c) are not satisfied. The penalty regulator $\epsilon_{DE,1}$ and $\epsilon_{DE,2}$ control how strictly the algorithm maintains the constraints, thereby balancing exploration and feasibility during the optimization process. The corresponding penalty functions in accordance with the objective function in (15) can be defined as

$$\omega(\chi_k) = \begin{cases}\chi_{min} - \chi_k, & \text{for } \chi_k < \chi_{min},\\ 0, & \text{for } \chi_k \geq \chi_{min},\end{cases} \tag{16a}$$

$$\rho(P_{id}) = \begin{cases}0, & \text{for } P < P_{max},\\ P - P_{max}, & \text{for } P \geq P_{max},\end{cases} \tag{16b}$$

where P_{id} denotes the total transmit power associated with the analog beamformer $\mathbf{W}_{A,id}$. In addition, we adopt the superiority feasible points (SFP) scheme [45] to ensure that infeasible individuals $\mathbf{W}_{A,x} \in P_{infs}$ in a population $P^{[\tau]}$ always have worse fitness values than feasible ones $\mathbf{W}_{A,y} \in P_{fs}$, with additional punishment $\eta(W_{A,id})$ given in (17), where $\mathcal{P}^{[\tau]} = \mathcal{P}_{fs}^{[\tau]} \cup \mathcal{P}_{infs}^{[\tau]}$. This guarantees that feasible solutions are always prioritized over infeasible ones during the selection process, thereby guiding the evolutionary search toward the feasible region of the solution space while maintaining population diversity.

Crossover: To enhance the diversity of the population, we merge the entries of each individual with those of its corresponding mutant matrix, potentially generating improved offspring solutions. To this end, a respective trial matrix $\mathbf{U}_{A,ind}^{[\tau]} \in \mathbb{C}^{N_T \times N_{RF}}$ is constructed for each individual under the control of a crossover rate C_r, defined as

$$\begin{aligned}&[\mathbf{U}_{A,id}]_{n,j}^{[\tau]}\\ &= \begin{cases}[\mathbf{V}_{A,id}^{[\tau]}]_{n,j} & \text{if } rand \leq C_r \text{ or } (n,j) = (n^*, j^*),\\ [\mathbf{W}_{A,id}^{[\tau]}]_{n,j} & \text{otherwise},\end{cases}\end{aligned} \tag{18}$$

where (n^*, j^*) denotes a randomly selected entry in the matrix to ensure at least one component is derived from $\mathbf{V}_{A,ind}$, thereby maintaining population diversity. Here, "$rand \in [0,1]$" indicates a uniformly distributed random number, sampled independently for each matrix entry.

Selection: During the selection phase, a new analog beamforming individual $\mathbf{W}_{A,ind}^{[\tau+1]}$ is formulated by comparing the fitness value of the corresponding trial matrix $\mathbf{U}_{A,id}^{[\tau]}$ against

$$\eta(W_{A,id}) = \begin{cases} \max\{0, \max_{\mathbf{W}_{A,y}\in\mathcal{P}_{fs}} f(\mathbf{W}_{A,y}) - \min_{\mathbf{W}_{A,x}\in\mathcal{P}_{infs}} F(\mathbf{W}_{A,x})\} & \text{if } \mathcal{P}_{fs} \neq \varnothing \text{ and } W_{A,id} \in \mathcal{P}_{infs}, \\ 0 & \text{otherwise.} \end{cases} \tag{17}$$

that of the target matrix $\mathbf{W}_{A,ind}^{[\tau]}$, as follows

$$\mathbf{W}_{A,id}^{[\tau+1]} = \begin{cases} \mathbf{U}_{A,id}^{[\tau]} & \text{if } \mathcal{F}(\mathbf{U}_{A,id}^{[\tau]}) < \mathcal{F}(\mathbf{W}_{A,id}^{[\tau]}), \\ \mathbf{W}_{A,id}^{[\tau]} & \text{otherwise.} \end{cases} \tag{19}$$

After evolving the candidate population through τ_{max} iterations of mutation, crossover, and selection, the DE algorithm yields an optimal analog beamformer $\mathbf{W}_A^{[t]} = \text{argmin}_{\mathbf{W}_{A,id}} \mathcal{F}$, for $\mathbf{W}_{A,id} \in \mathcal{P}^{[\tau_{max}]}$.

B. VQO-Based Digital Beamformer Design.

1) Preliminaries on Quantum Computing: Unlike conventional computing, where a classical bit represents either state 0 or 1, quantum computing utilizes quantum bits, or qubits, which leverage the principles of quantum mechanics to exist in a superposition of the two computational basis states, denoted in Dirac notation as $|\psi\rangle = p_0|0\rangle + p_1|1\rangle$, where $|0\rangle = [1,0]^T$ and $|1\rangle = [0,1]^T$. Here, $|p_0|^2$ and $|p_1|^2$ represent the probability of measuring the qubit in states 0 and 1, respectively, where $|p_0|^2 + |p_1|^2 = 1$. While a classical system of n bits can only process one of the 2^n possible sequences $\{\underbrace{0...00}_{\text{n bits}}, 0...01, \ldots, 1...11\}$ at a time, an n-qubit quantum register can exploit superposition to represent all 2^n states simultaneously. The corresponding superposition state can be described as

$$|\psi\rangle = \sum_{i=0}^{2^n-1} p_i |i\rangle, \tag{20}$$

where p_i corresponds to the probability amplitude of the basis state $|i\rangle$. This exponential growth in representational capacity enables quantum algorithms to explore large solution spaces in parallel, accelerating convergence to optimal solutions in complex optimization problems.

Quantum computation operates through quantum circuits that implement algorithms using quantum gates. These gates are unitary operators that act on quantum states, guiding their evolution toward a final state from which the desired classical information can be obtained. To create superposition states from the computational basis $\{|0\rangle, |1\rangle\}$, a common approach is to apply the Hadamard gate, which transforms these basis states according to

$$H : |0\rangle \mapsto \frac{1}{\sqrt{2}}(|0\rangle + |1\rangle), \tag{21}$$

$$H : |1\rangle \mapsto \frac{1}{\sqrt{2}}(|0\rangle - |1\rangle), \tag{22}$$

where its matrix representation is

$$H = \frac{1}{\sqrt{2}} \begin{bmatrix} 1 & 1 \\ 1 & -1 \end{bmatrix}. \tag{23}$$

This operator creates equal-amplitude superpositions, which is essential for initializing quantum algorithms. In addition, rotation gates can be employed to perform rotations of a qubit's state on the Bloch sphere. Specifically, R_Y and R_Z rotate the qubit around the y- and z-axes of the Bloch sphere, respectively, and can be expressed as

$$R_Y(\theta) = \begin{bmatrix} \cos(\frac{\theta}{2}) & -\sin(\frac{\theta}{2}) \\ \sin(\frac{\theta}{2}) & \cos(\frac{\theta}{2}) \end{bmatrix}, \tag{24a}$$

$$R_Z(\theta) = \begin{bmatrix} e^{-i\frac{\theta}{2}} & 0 \\ 0 & e^{i\frac{\theta}{2}} \end{bmatrix}. \tag{24b}$$

While R_Y is capable of adjusting the probability amplitude distribution, R_Z provides relative phase-shift control. Besides single-qubit gates, multi-qubit gates allow one qubit to control the operation on another. Specifically, CNOT is a fundamental two-qubit quantum gate that introduces the entanglement property, which allows quantum computers to perform vast calculations simultaneously [46]. It flips the target $(q+1)$-th qubit if the control q-th qubit is in state $|1\rangle$, and leaves the target qubit unchanged otherwise. Its operation can be mathematically represented as

$$CNOT = \frac{1}{\sqrt{2}} \begin{bmatrix} 1 & 0 & 0 & 0 \\ 0 & 1 & 0 & 0 \\ 0 & 0 & 0 & 1 \\ 0 & 0 & 1 & 0 \end{bmatrix}. \tag{25}$$

2) Variational Quantum Optimizer: A variational quantum circuit exploits the capabilities of quantum gates by using parameterized gates that depend on trainable parameters. By employing a VQC with a classical optimizer, typically a gradient-based method, a variational quantum optimizer (VQO) is formulated to fine-tune these parameters, enabling the system to learn the optimal solutions to complex problems. A VQC comprises three main layers: data encoding layer, parameterized layer, and measurement layer. Data encoding layer acts as an interface that maps the classical information into quantum states by applying quantum operations that encode classical input values into the amplitudes or phases of qubits. In the parameterized layer, multiple rotation and entangling gates are employed to manipulate the qubits, with each rotation controlled by a tunable classical parameter. By adjusting these rotation angles, the layer can modify the quantum state in a flexible and trainable way. To extract information from the circuit, the resulting quantum states are measured using quantum measurement operations, which collapse them into usable classical data. The details of the employed VQO in this paper will be discussed below.

Initialization: The first stage of the VQC is the encoding layer, where the classical channel information $\mathbf{H}_K$ and the analog precoder $\mathbf{W}_A$ from III-A are mapped into a quantum reference state. Specifically, we compute $\mathbf{G}_{KN_{RF}}^{[t]} = \mathbf{H}_K^H \mathbf{W}_A^{[t]}$ and then flatten the matrix into $\mathbf{G}_f^{[t]} = \{\mathbf{x}_1, \ldots, \mathbf{x}_{KN_{RF}}\}$. The reference state is obtained by encoding the classical

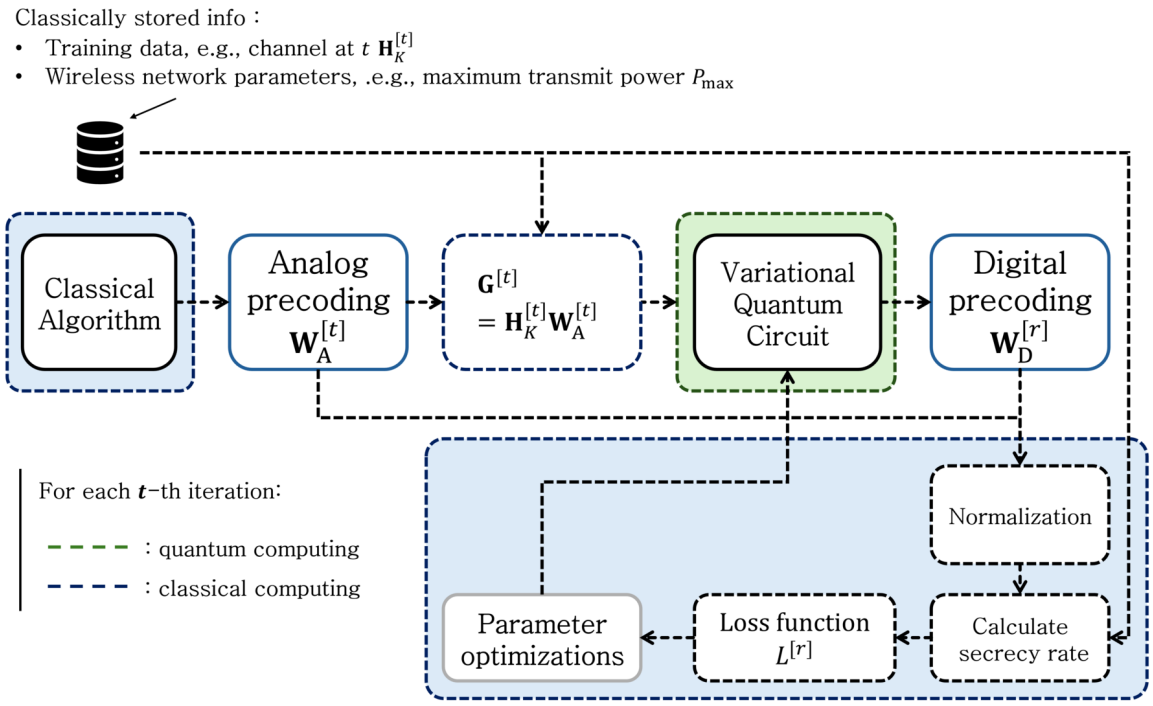

Fig. 4. Workflow overview of the proposed SQC algorithm.

information $\mathbf{x}_q \in \mathbf{G}_f^{[t]}$ into the computational basis state $|0\rangle^{\otimes Q}$ as $|\psi_r\rangle = U_E |0\rangle^{\otimes Q}$, where U_E is the encoding operator, defined as

$$U_E = \bigotimes_q^{Q/2} R_Y^{(2q-1)}(\mathcal{R}(\mathbf{x}_q)) R_Z^{(2q)}(\mathcal{I}(\mathbf{x}_q)) H^{\otimes Q}, \tag{26}$$

where $Q = 2N_{RF}K$ denotes the number of qubits. First, Hadamard gates map the ground state $|0\rangle^{\otimes Q}$ into a uniform superposition state, as follows

$$|\psi_1\rangle = H^{\otimes Q}|0\rangle^{\otimes Q} = \frac{1}{\sqrt{2^Q}} \sum_{x=0}^{2^Q-1} |x\rangle, \tag{27}$$

where all the computational basis states have the same probability of $\frac{1}{2^Q}$, which allows exploration of all the solutions concurrently. Then, the classical information are encoded as rotation angles in R_Y and R_Z gates, which act as an interface between the classical and quantum realms. Under the operation of the encoding scheme, the reference state provides initial guidance for the VQC, thereby significantly accelerating the quantum learning process.

Training: In the following, we discuss the iterative training procedure of the VQC parameters to generate the desired quantum states that yield effective digital beamforming matrices. This process employs a gradient-based optimizer to adjust the rotation angles of the quantum gates to maximize the total secrecy rate while satisfying the system constraints in (13b)-(13d). In the parameterized layer, the initial reference state is transformed through a trainable, parameterized unitary operator U_P with multiple parameterized layer, $U^{(\ell)}$, producing the parameterized state

$$|\psi_p\rangle = U_P(\boldsymbol{\theta})|\psi_r\rangle = \prod_{\ell=1}^{\mathcal{L}} U_P^{(\ell)}(\boldsymbol{\theta}_\ell)|\psi_r\rangle, \tag{28}$$

where $\mathcal{L}$ denotes the number of layers. The operation on each layer is constructed using the rotation gate R_Y and the controlled-NOT (CNOT) gate, as in the following.

$$U_P^{(\ell)} = U_{ent}^{(\ell)} \cdot U_{rot}^{(\ell)}, \tag{29}$$

where

$$U_{ent}^{(\ell)} = \prod_{q=1}^{Q} \mathrm{CNOT}_{(q,\,(q+1) \bmod Q)}, \tag{30}$$

and

$$U_{rot}^{(\ell)} = \bigotimes_{q=1}^{Q} R_Y^{(q)}(\theta_{\ell,q}). \tag{31}$$

$U_{ent}^{(\ell)}$ and $U_{rot}^{(\ell)}$ represent the entangling and learnable rotational operations, respectively, within each layer ℓ. During the training process, the trainable parameter $\boldsymbol{\theta}$ is optimized to achieve an optimal state $|\psi_p^*\rangle$. This sophisticated multilayer structure enhances the expressibility of the circuit and its ability to approximate complex states, while preventing premature convergence to local minima [47]. However, as the number of parameterized layers increases, the optimization domain tends to experience the barren plateau effect, wherein the objective function becomes exceedingly flat, causing the gradient to vanish exponentially with respect to the number of qubits [48]. This trade-off between expressibility and trainability requires a careful selection of the number of parameterized

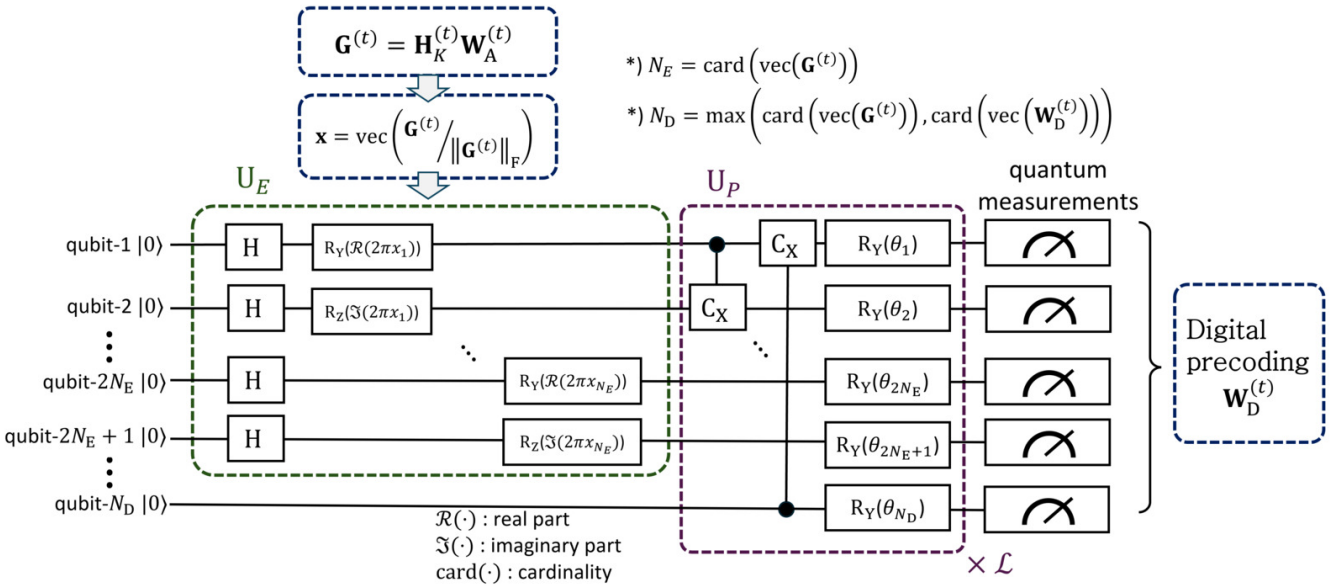

Fig. 5. Proposed VQO-based digital beamformer design

layers, ensuring optimal convergence without compromising optimization efficiency. The employed VQO is illustrated in Fig. 5. In each iteration r, the parameterized state $|\psi_P\rangle$ is measured by the Pauli-Z operator, represented as

$$Z = \begin{bmatrix} 1 & 0 \\ 0 & -1 \end{bmatrix}, \tag{32}$$

which projects the state onto $|0\rangle$ and $|1\rangle$, yielding an expectation value

$$\langle Z_d \rangle = \sum_{i=0}^{2^Q-1} |c_i|^2 (-1)^{i_d}, \tag{33}$$

where c_i are the amplitudes of the computational basis states $|i\rangle$ in $|\psi_P\rangle$ and i_d denotes the d-th bit of $|i\rangle$. This measurement collapses the qubit pairs $(2q-1, 2q)$ into classical information $\mathcal{R}(\mathbf{z}_{j,k})$ and $\mathcal{I}(\mathbf{z}_{j,k})$, respectively, where $\mathbf{z}_{j,k}$ is a matrix entry of the digital beamformer $\mathbf{W}_D^{[r]}$, for $j \in \{1, \ldots, N_{RF}\}$ and $k \in \{1, \ldots, K\}$. The circuit's measurement output is utilized to minimize the loss function, defined as

$$\mathsf{L}^{(r)} = -\sum_{k=1}^{K} \chi_k - \sum_{k=1}^{K} \vartheta_{\text{rate}}(\chi_k) - \frac{\chi_M}{\chi_{min}} \chi_m, \tag{34}$$

where the second term imposes a log-barrier penalty to enforce compliance with the constraint defined in (13b). This penalty function can be described as

$$\vartheta_{\text{rate}}(\chi_k) = \epsilon_{VQO} \log(\max(\chi_k, \beta)), \tag{35}$$

where β denotes the punishment factor (i.e., $\beta = 10^{-8}$). In addition, the third term maintains the fairness between the highest and lowest user rates, denoted by χ_M and χ_m, respectively, once (13b) is not satisfied. Whenever an undesired early termination $\sum_i \chi_i = 0$ occurs, we reinitialize the training process with different starting point. The adopted log-barrier penalty function does not guarantee strict satisfaction of the QoS constraints throughout the optimization process. Instead, it assigns a significantly large penalty to infeasible solutions, which discourages constraint violations and guides the optimizer toward the feasible region. To promote balanced performance and mitigate bias, the fairness term is formulated such that any violation of requirements forces the objective to prioritize the contribution of the minimum-rate user, effectively encouraging the optimizer to improve its performance. At the end of each iteration, gradient-based optimizer employs parameter-shift rule to optimize the learnable parameter $\boldsymbol{\theta}$. The gradient of the loss function $\mathsf{L}^{(r)}$ with respect to each circuit parameter $\theta_{\ell,m}$ is given by [49]

$$\frac{d\mathsf{L}^{(r)}}{d\theta_{\ell,m}} = \frac{1}{2}\left[\mathsf{L}^{(r)}\left(\theta_{\ell,m} + \varrho\right) - \mathsf{L}^{(r)}\left(\theta_{\ell,m} - \varrho\right)\right], \tag{36}$$

where ϱ denotes non-zero shift variable, e.g., $\frac{\pi}{2}$. After computing the gradients via the parameter-shift rule, the parameter $\boldsymbol{\theta}$ is updated to minimize the objective function $\mathsf{L}^{(r)}$ in the next iteration. This iterative procedure proceeds for r_{max} iterations, enhancing the quantum state $|\psi_P\rangle$ to produce an optimal digital beamformer while respecting the fairness and constraint conditions. Of note, the proposed VQO framework starts from an initial feasible solution, which further supports convergence toward constraint-compliant solutions.

Obtaining the digital beamforming matrix: Given the output vector of the quantum learning model at iteration r as $\mathbf{z}^{[r]} = [z_q^{[r]}]_{q=1}^{Q}$, where $z_q^{[r]} \in [-1, 1]$, each (i, j)-th element of the digital beamforming matrix $\mathbf{W}_D^{[r]}$ can be obtained as: $\mathbf{w}_{j,k}^{[r]} = z_{2q-1} + i z_{2q}$ for $q \in \{1, \ldots, \frac{Q}{2}\}$, $\mathbf{w}_{j,k}^{[r]} \in \mathbf{W}_D^{[r]}$, $\forall j, k$. Ensuring (13b) is satisfied, $\mathbf{W}_D^{[r]} \leftarrow \frac{P_{max}\mathbf{W}_D^{[r]}}{\|\mathbf{W}_A^{[0]}\mathbf{W}_D^{[r]}\|_F}$ [50]. The resulting digital beamformer $\mathbf{W}_D^{[r]}$ can be directly used for the objective in (13a).

IV. Simulation Results and Discussion

A. Simulation Results

In this section, we provide the simulation results for the proposed hybrid quantum-classical workflow. The BS uses an ELAA of $N_T = 257$ elements along the x-axis. The communication process employs a carrier frequency of 30 GHz (i.e., $\lambda = 1$ cm) with the adjacent antenna spacing of half-wavelength. We set the noise power and the maximum power allocation to $\sigma^2 = -105$ dBm and $P_{max} = 30$ dBm, respectively. All the legitimate users are required to achieve the QoS requirement of $\chi_{min} = 1.0$ bps/Hz. When the minimum QoS requirement of the legitimate users increases, the sum secrecy rate typically decreases. This is because stricter QoS constraints limit the feasible solution space for the optimization, thus reducing the degrees of freedom available for enhancing secrecy rates.

The transmitter simultaneously serves two legitimate users at $(20\text{m}, 30°)$ and $(20\text{m}, 60°)$ while avoiding the interception from an eavesdropper at $(10\text{m}, 30°)$. This setup assumes that both the legitimate users and the eavesdropper share the same transmission direction, which challenges the effectiveness of LDMA. In such scenarios, SDMA may be inadequate to provide precise spatial resolution as its beamsteering can limit the system's ability to isolate users in the spatial domain [8]. We consider a realistic multi-path model which involves $L = 3$ NLoS paths.

The population size M of DE is balanced to ensure sufficient diversity for obtaining the optimal high-dimensional analog precoder W_A without incurring a high computational overhead [51]. The differential weight factor ζ is initially set to 0.5 to control mutation amplification, while the crossover rate Cr is typically started at 0.9 to promote rapid convergence [52], [53]. These parameters are then iteratively adjusted, i.e., increasing ζ for diversity or reducing Cr for stability, to maintain a proper trade-off between convergence speed and the risk of generating infeasible individuals [54]. The penalty regulators $\epsilon_{DE,1}, \epsilon_{DE,2}$, and ϵ_{VQO} are empirically tuned to penalize constraint violations, starting with small values that gradually increase until the algorithm consistently converges to feasible solutions while maintaining good objective performances [55], [56]. The learning rate α of VQO is determined through empirical observation to find the optimal balance between avoiding divergence and ensuring a practical convergence speed [57]. In particular, the DE and VQO parameters are listed in Table I. DE phase employs a population of $M = 20$ individuals to ensure sufficient diversity within the search space for analog beamformer and to accelerate the convergence process. Penalty regulators, i.e., $\epsilon_{DE,1} = 200$, $\epsilon_{DE,2} = 2 \times 10^4$, and $\epsilon_{VQO} = 0.5$ guarantee QoS and power allocation requirements. VQO employs Adam optimizer to optimize $\boldsymbol{\theta}$ using the parameter-shift rule, with a learning rate of $\alpha = 0.05$.

Besides our proposed approaches, we analyze the performance of other models, as described in the following.

- Proposed sequential quantum-classical (SQC) algorithm: Jointly designs the analog and digital beamformers to achieve an optimal sum secrecy rate. The analog beamformer is optimized using the DE algorithm, while the digital beamformer is enhanced through the VQO in Fig. 5.
- Reduced-layout sequential quantum-classical (R-SQC) algorithm: A variant of the SQC that retains the same DE-based optimization for the analog beamformer but employs a reduced-layout variational quantum circuit (R-VQC) with fewer qubits, as shown in Fig 6, to optimize the digital beamformer, thereby lowering computational complexity.
- Iterative differential evolution (IDE) algorithm: Utilizes the nature-inspired operators of the DE technique (comprising of mutation, crossover, and selection) to iteratively optimize the analog and digital beamformers. This optimization approach aims to enable an efficient hybrid beamforming design, with both phases implemented using classical methods.
- Differential evolution-based analog beamformer (DE-AB): Employs the DE algorithm to adjust the phase shifters of the analog beamformer, while the digital beamformer is initialized randomly.
- Maximum ratio transmission (MRT): Maximizes the received signal power at each intended user, with beamforming vectors defined as $\mathbf{w}_k = \frac{\mathbf{h}_k}{\|\mathbf{h}_k\|}$.
- Fully-digital zero-forcing (ZF): This scheme eliminates inter-user interference through fully-digital precoding, expressed as $\mathbf{W} = \mathbf{H}_K^H(\mathbf{H}_K\mathbf{H}_K^H)^{-1}$.

TABLE I
Hyperparameter settings for Algorithm 1

Parameters	Value
Max SQC epochs t_{max}	10
Max DE generations τ_{max}	20
DE individuals M	20
Max VQO iterations r_{max}	100
DE secrecy penalty regulator $\epsilon_{DE,1}$	200
DE power penalty regulator $\epsilon_{DE,2}$	2×10^4
Differential weight factor ζ	0.5
Crossover rate C_r	0.5
Number of qubits Q	8
VQO penalty regulator ϵ_{VQO}	0.5
VQO learning rate α	0.05

The R-SQC algorithm, illustrated in Fig. 6, utilizes only half the number of qubits used in the proposed SQC. The primary distinction between R-SQC and the proposed SQC lies in the encoding layer U_E and the post-measurement output processing. Unlike the proposed SQC, where the real and imaginary components of each element in $\mathbf{G}^{(t)}$ are encoded separately, the R-SQC circuit integrates both components within a single qubit. This is accomplished by sequentially applying $R_Y(2\pi\mathcal{R}(\mathbf{x}_{j,k}))$ and $R_Z(2\pi\mathcal{I}(\mathbf{x}_{j,k}))$ rotations to the same qubit, where $2\pi\mathcal{R}(\mathbf{x}_{j,k})$ and $2\pi\mathcal{I}(\mathbf{x}_{j,k})$ denote the rotation angles, effectively reducing the number of qubits by

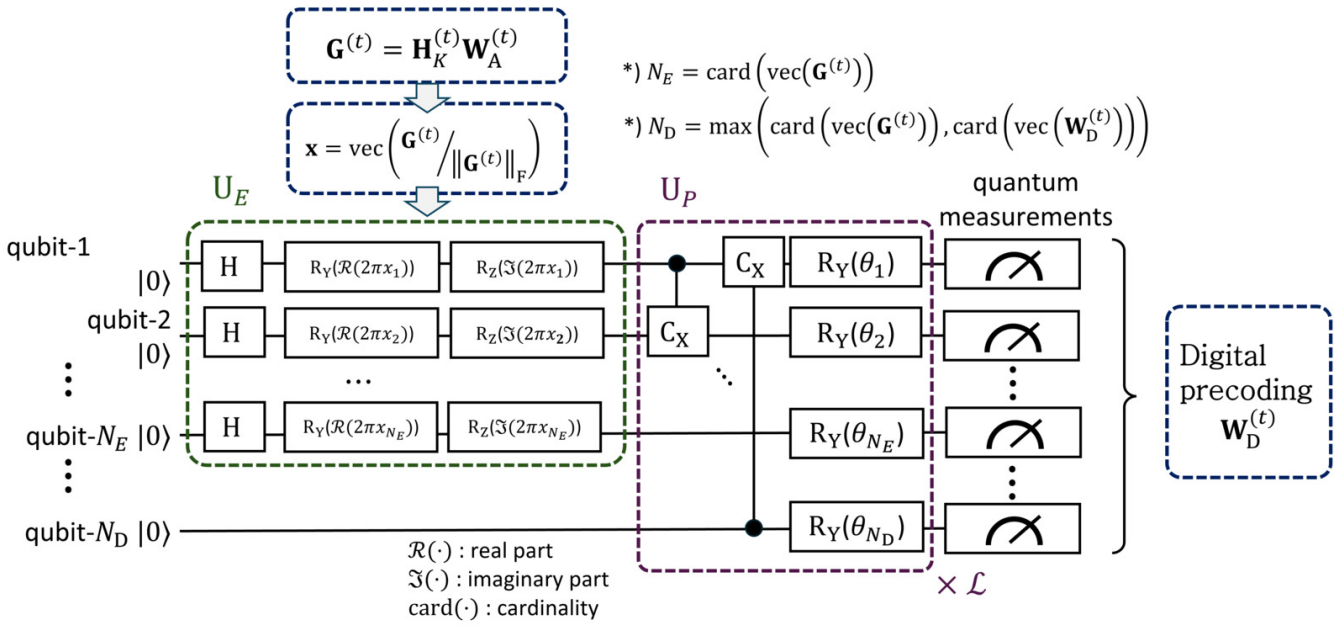

Fig. 6. Reduced-layout VQO-based digital beamformer design.

half. The circuit output $\mathbf{z}$ is then used to build the digital beamforming element $w_{j,k}^{[r]} = \exp(2\pi z_q^{[r]})$, and the magnitude of each entry is normalized in the same manner as in the SQC. With this configuration, R-SQC substantially reduces quantum resource utilization and computational complexity. However, this reduction comes at the expense of lower circuit expressibility, limiting its ability to achieve the optimal solution.

Fig. 7 illustrates the convergence performance of the proposed and baseline schemes. The proposed SQC algorithm achieves an early convergence with the highest secrecy performance. For instance, it attains the secrecy rates of approximately 24.5 bps/Hz as early as the first and second iterations. In comparison, DE-AB only achieves the secrecy rates of about 12 bps/Hz at the same iterations. Although the IDE and DE-AB schemes outperform conventional benchmarks (MRT and ZF), their convergence is slower, yielding a secrecy rate approximately 20% to 30% lower than that of the proposed SQC solution. This demonstrates that the proposed SQC algorithm can efficiently solve the joint optimization problem of system performance and power allocation, emphasizing the computational advantages and convergence speedup provided by quantum computing. This is especially helpful for scenarios demanding quick optimization with limited numbers of iterations, such as in low latency communications and/or real-time environments.

Fig. 8 compares the secrecy rates of the five approaches with respect to the total transmit power of the BS. At low transmit power, i.e., $P_{max} \leq 20$ dBm, the proposed SQC achieves approximately the same secrecy rate as IDE and DE-AB. However, as the transmit power increases, SQC outperforms these two schemes by effectively leveraging power allocation and LDMA to mitigate inter-user interference and direct the signal toward the intended users. At high transmit power, IDE underperforms due to its slower convergence in refining the

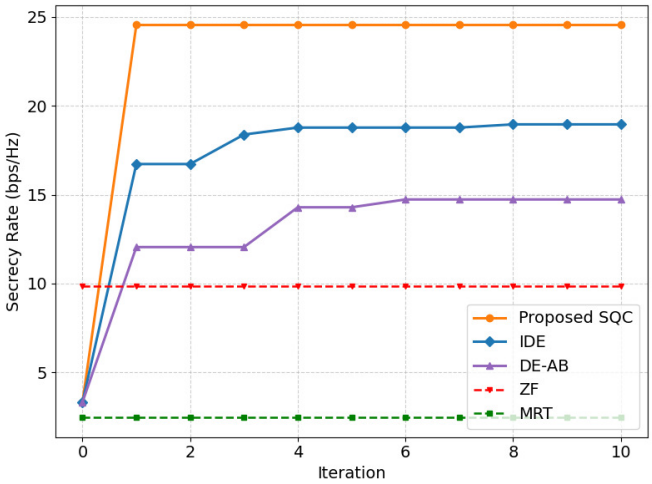

Fig. 7. Secrecy rate performance of the proposed schemes against eavesdropping threat.

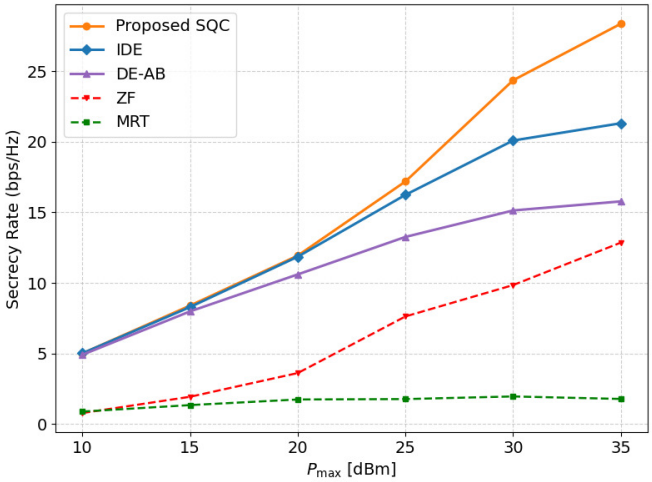

Fig. 8. Secrecy rates versus the maximum power allocation values.

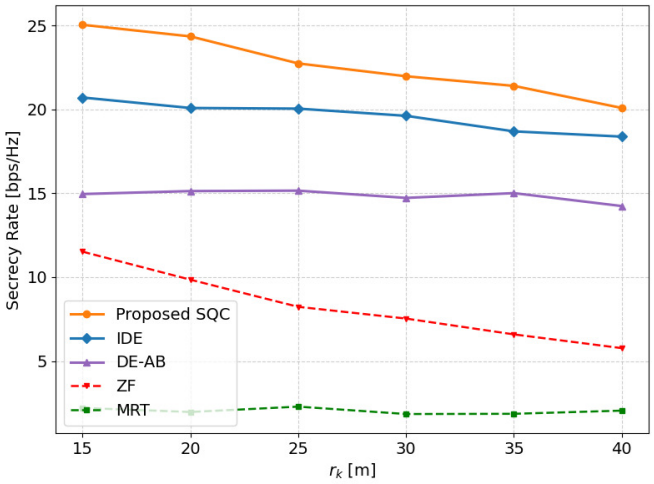

Fig. 9. Secrecy rates with respect to the user distances.

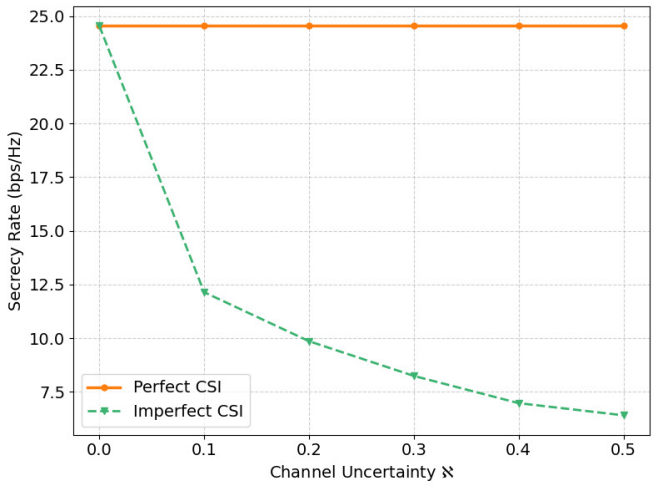

Fig. 10. Performance of SQC workflow under different channel conditions.

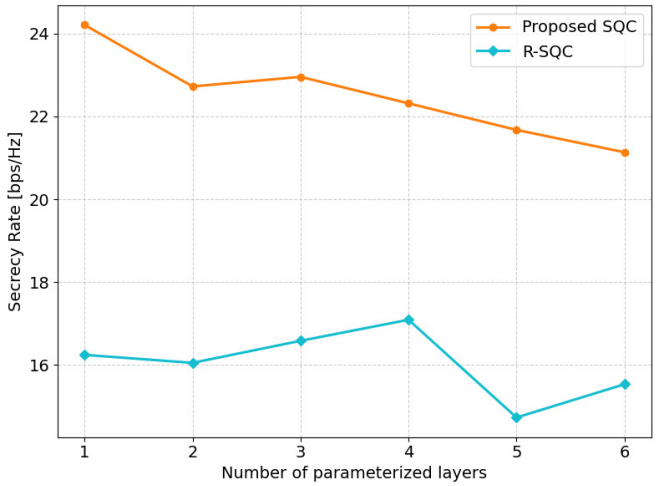

Fig. 11. Secrecy rates with respect to the numbers of parameterized layers.

hybrid beamforming architecture with a fixed number of individuals in the population. This limitation prevents IDE from fully exploiting the available power for optimal performance, resulting in reduced secrecy rates compared to SQC.

Fig. 9 shows the relationship between the distance of users to the BS with the total secrecy rate. The proposed SQC algorithm outperforms all other benchmarks, exhibiting the highest secrecy rate, particularly when users are in close proximity to the BS. SQC maintains a strong performance with only a moderate decrease as the user moves farther from the BS. Similarly, IDE experiences a slight downward trend as the channel conditions worsen owing to signal attenuation with increasing distance. Meanwhile, DE-AB shows relatively stable secrecy performance which depends on the digital beamforming initialization. MRT scheme, however, fails to ensure secure connections between the BS and users, as it is unable to effectively mitigate the eavesdropping threat, resulting in significantly lower secrecy rates across the distance range. Such results highlight the suitability of learning model-based approaches to maintain PLS despite unfavorable BS-user distances. Even at a distance of 40 meters, SQC outperforms MRT-based approach.

In NFC systems, precise acquisition of CSI is essential for enhancing beamforming design and ensuring secure connections. However, in practice, the integrity of CSI is often compromised by pilot contamination and the non-stationary nature of high-frequency propagation [58]. To evaluate the robustness of the proposed SQC workflow in such conditions, we adopted a bounded CSI error model for the BS-user channel [59]. The imperfect channel model pertaining to each k-th user, $\hat{\mathbf{h}}_k$, $\forall k$, can be expressed as

$$\hat{\mathbf{h}}_k = \mathbf{h}_k - \Delta\mathbf{h}_k, \tag{37}$$

where $\Delta\mathbf{h}_k$ represents the estimation error, which is independent of h_k, satisfying the below condition

$$\|\Delta\mathbf{h}_k\|_2 \leq \aleph\|\mathbf{h}_k\|_2. \tag{38}$$

Here, $\aleph \in [0, 1)$ denotes the level of channel uncertainty where $\aleph = 0$ corresponds to the case of perfect CSI.

Fig. 10 illustrates the secrecy performance of the proposed SQC algorithm under different channel conditions: perfect and imperfect CSI. Under perfect CSI, the proposed algorithm attains high secrecy rate which allows robust and secure communication. However, in imperfect conditions, as the uncertainty level $\aleph$ increases, the secrecy performance degrades significantly due to the lack of accurate channel information. Notably, even at a high uncertainty level of $\aleph = 0.5$, the proposed scheme still achieves approximately 6.5 bps/Hz, which is moderately higher than the MRT scheme, demonstrating its superior resilience under adverse channel conditions.

Fig. 11 investigates the effect of quantum circuit complexity on system security performance. The proposed SQC consistently achieves higher secrecy rates compared to the R-SQC across all circuit depths, showing its superior ability in enhancing communication security. The performance gain mainly results from employing a larger number of qubits in the proposed VQC, allowing flexible control over both real and imaginary components of the beamforming weights. While increasing the number of layer provides expressibility in achieving more complex quantum states, as observed around four layers in R-SQC, this improvement does not always translate into better secrecy performance. Beyond a certain

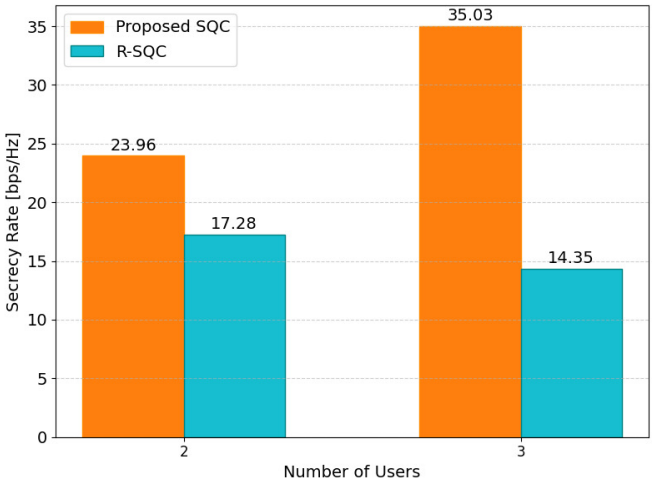

Fig. 12. Secrecy rates given the numbers of users.

circuit depth, the optimization domain of the proposed VQC tends to become more rugged, leading to barren plateau regions where gradient magnitudes vanish. Moreover, high-complexity quantum circuit accumulate gate errors and decoherence effects, reducing the system security performance [60]. This expressibility–trainability trade-off is evident in the performance trend of the proposed SQC, where even a single parameterized layer is sufficient to achieve optimal secrecy performance.

Fig. 12 illustrates the performance of the proposed SQC and R-SQC schemes in a multi-user scenario. As the number of users increases, the resulting mutual interference becomes more significant. Under these conditions, the proposed SQC scheme consistently achieves a higher secrecy rate, whereas its counterpart experiences performance degradation. These results demonstrate the effectiveness of the proposed approach in efficiently allocating resources to maintain secure links in multipath NFC environment. Furthermore, they highlight the scalability and robustness of the proposed solution in handling increased user density. This finding is beneficial to anticipate pertinent factors such as: i) the expected growth in the total number of users and ii) the increase in the number of devices as new devices enter the service area.

B. Further Discussion

Scalability: As the number of antennas N_T increases, the number of qubits and circuit depth of the VQC remain unchanged. Specifically, these quantum computational resources, which are used to optimize the digital precoder $\mathbf{W}_D \in \mathbb{C}^{N_{RF}\times K}$, solely depend on the number of existing legitimate users K and the number of employed radio-frequency chains N_{RF}. However, scaling of ELAA moderately impacts the DE algorithm. Each candidate solution in the population corresponds to a potential analog precoder $\mathbf{W}_A \in \mathbb{C}^{N_T\times N_{RF}}$, whose dimensionality scales linearly with the number of antennas N_T. Consequently, as N_T increases, the size of $\mathbf{W}_A$ grows, leading to a larger search space and higher computational overhead.

Efficiency: In the proposed SQC workflow, the classical DE algorithm is used to optimize the analog precoder, while the VQO is utilized only for the digital precoding stage. DE is a population-based global optimization algorithm that does not rely on convexity assumptions and can directly handle the original non-convex problem. While VQO has potential for wireless optimization, it may require larger quantum resources (particularly more qubits) as the number of antennas increases. This limitation is further constrained by the restricted number of qubits available in current NISQ devices. Therefore, integrating DE can aid in reducing the required number of qubits, and provide a more practical solution for optimizing analog precoding in the considered system.

The proposed algorithm significantly reduces the required number of qubits and circuit depth compared with approaches that rely entirely on VQCs to optimize both digital and analog precoders. In a fully VQC-based implementation, the required quantum resources scale linearly with the number of antennas in the ELAA and the number of RF chains. Table II compares the quantum resource required by the proposed methods and fully-VQC implementation where $\mathcal{L}$ indicates the number of parameterized layers. As the number of antennas scales to thousands in realistic ELAA systems, this would require a substantial number of qubits, which remains a major bottleneck for current NISQ devices. As the number of antennas of ELAA is much larger than that of users in a massive MIMO system, i.e., $N_T \gg K$, the fully-VQC implementation requires substantial quantum resource in comparison with its counterparts. While R-SQC requires approximately half the quantum resource of the proposed SQC, its performance degrades as the number of users increases.

V. Conclusion

This paper leverages the LDMA technique in NFC to support multi-user transmissions, and proposes a sequential quantum-classical (SQC) workflow to optimize hybrid beamforming design. In particular, the study aims to maximize the sum secrecy rate by jointly optimizing both digital and analog precoding, while satisfying power allocation constraints and QoS requirements. Exploiting the superposition and entanglement of quantum computing, we employ VQC to optimize the digital beamfomring design. To efficiently leverage quantum resources and enhance the overall performance, we integrate the nature-inspired differential evolution algorithm to alleviate the high-dimensional analog beamforming design. The simulation results show that the proposed algorithm provides a superior secrecy rate compared to other benchmarks and demonstrates faster convergence. This paper therefore exhibits the potential of hybrid quantum-classical workflows for PLS in NFC, promoting the security in 6G networks.

This work focuses on a single eavesdropper intercepting signals from all legitimate users. Considering scenarios with multiple eavesdroppers, while ensuring the minimum QoS requirements of legitimate users, represents an important direction for future research. Specifically, the objective function can be adapted to account for multiple eavesdroppers, while the minimum QoS constraints must still be guaranteed for each user with respect to each eavesdropper. For future work, scenarios involving mobile scatterers, which result in non-stationary multipath propagation, can be investigated. Another

TABLE II
QUANTUM RESOURCE REQUIREMENTS FOR DIFFERENT METHODS

	SQC	**R-SQC**	**Fully-VQC**
Number of qubits	$2N_{RF}K$	$N_{RF}K$	$2N_{RF}(K+N_T)$
Number of Hadamard gates	$2N_{RF}K$	$N_{RF}K$	$2N_{RF}(K+N_T)$
Number of Rotational gates	$2N_{RF}K(\mathcal{L}+1)$	$N_{RF}K(\mathcal{L}+2)$	$2N_{RF}(K+N_T)(\mathcal{L}+1)$
Number of CNOT gates	$2N_{RF}K\mathcal{L}$	$N_{RF}K\mathcal{L}$	$2N_{RF}(K+N_T)\mathcal{L}$

promising direction for future work is to extend the proposed SQC workflow to cooperative, relay-assisted NFC systems, which offer additional spatial degrees of freedom to improve the secrecy rate, particularly in environments with high node density. By jointly optimizing the full-duplex relay selection and the SQC-based beamforming design, the system may achieve higher secrecy gains while maintaining efficient energy use, even under varying channel conditions.

REFERENCES

[1] C.-X. Wang, X. You, X. Gao, X. Zhu, Z. Li, C. Zhang *et al.*, "On the road to 6G: Visions, requirements, key technologies, and testbeds," *IEEE Commun. Surv. Tutor.*, vol. 25, no. 2, pp. 905–974, Apr. 2023.

[2] I. Batool, M. M. Fouda, M. Ismail, M. I. Ibrahem, K. Rabie, S. Verma, and Z. M. Fadlullah, "Joint optimization of IRS and THz resource allocation in 6G IoT networks: An adaptive online MADDPG approach," *IEEE Internet Things J.*, vol. 12, no. 22, pp. 47 118–47 134, 2025.

[3] S. Sharma, P. K. Singya, K. Deka, C. Adjih, and M. Sharma, "Terahertz communication: State-of-the-art and future directions," *IEEE Open J. Commun. Soc.*, vol. 6, pp. 6281–6322, Jan. 2025.

[4] S. Verma, T. K. Rodrigues, N. Kato, M. M. Fouda, and M. Ismail, "Empirical analysis of statistical variation in channel data of WiGig networks towards 6G," in *2025 IEEE 101st Vehicular Technology Conference*, Oslo, Norway, Jun. 2025, pp. 1–5.

[5] S. Ye, M. Xiao, M.-W. Kwan, Z. Ma, Y. H. G. Karagiannidis *et al.*, "Extremely large aperture array (ELAA) communications: Foundations, research advances and challenges," *IEEE Open J. Commun. Soc.*, vol. 5, pp. 7075–7120, Oct. 2024.

[6] W. Saad, M. Bennis, and M. Chen, "A vision of 6G wireless systems: Applications, trends, technologies, and open research problems," *IEEE Netw.*, vol. 34, no. 3, pp. 134–142, May 2020.

[7] H. Zhang, N. Shlezinger, F. Guidi, D. Dardari, M. F. Imani, and Y. C. Eldar, "Beam focusing for near-field multiuser MIMO communications," *IEEE Trans. Wireless Commun.*, vol. 21, no. 9, pp. 7476–7490, Sep. 2022.

[8] Z. Wu and L. Dai, "Multiple access for near-field communications: SDMA or LDMA?" *IEEE J. Sel. Areas Commun.*, vol. 41, no. 6, pp. 1918–1935, Jun. 2023.

[9] Y. Liu, Z. Wang, J. Xu, C. Ouyang, X. Mu, and R. Schober, "Near-field communications: A tutorial review," *IEEE Open J. Commun. Soc.*, vol. 4, pp. 1999–2049, Aug. 2023.

[10] Y. Liu, J. Xu, Z. Wang, X. Mu, and L. Hanzo, "Near-field communications: What will be different?" *IEEE Wirel. Commun.*, vol. 32, no. 2, pp. 262–270, Apr. 2025.

[11] H. Zhang, N. Shlezinger, F. Guidi, A. Guerra, D. Dardari, and M. F. Imani, "Near-field beam focusing for wireless power transfer with dynamic metasurface antennas," *IEEE Internet Things J.*, vol. 12, no. 12, pp. 18 596–18 605, Jun. 2025.

[12] ITU-R, *Framework and overall objectives of the future development of IMT for 2030 and beyond*, International Telecommunication Union, Radiocommunication Sector (ITU-R) Recommendation M.2160-0, Nov. 2023.

[13] 3GPP, *Security architecture and procedures for 5G System*, 3rd Generation Partnership Project (3GPP) Technical Specification (TS) TS 33.501, Nov. 2025.

[14] X. Chen, D. W. K. Ng, W. H. Gerstacker, and H.-H. Chen, "A survey on multiple-antenna techniques for physical layer security," *IEEE Commun.*, vol. 19, no. 2, pp. 1027–1053, Nov. 2017.

[15] L. Lv, D. Xu, R. Q. Hu, Y. Ye, and L. Y. X. Lei, "Safeguarding next-generation multiple access using physical layer security techniques: A tutorial," *Proc. IEEE*, vol. 112, no. 9, pp. 1421–1466, Jul. 2024.

[16] L. Mucchi, S. Jayousi, S. Caputo, E. Panayirci, S. Shahabuddin, J. Bechtold *et al.*, "Physical-layer security in 6G networks," *IEEE Open J. Commun. Soc.*, vol. 2, pp. 1901–1914, Aug. 2021.

[17] M. H. Khoshafa, T. M. N. Ngatched, M. H. Ahmed, and A. Ibrahim, "Improving physical layer security of cellular networks using full-duplex jamming relay-aided D2D communications," *IEEE Access*, vol. 8, pp. 53 575–53 586, Mar. 2020.

[18] Z. Zhang, Y. Liu, Z. Wang, X. Mu, and J. Chen, "Physical layer security in near-field communications," *IEEE Trans. Vehi. Technol.*, vol. 73, no. 7, pp. 10 761–10 766, Jul. 2024.

[19] B. Zhuo, J. Gu, G. Zhang, and H. Yang, "Imperfect resolution of near-field beamfocusing for NOMA-aided physical-layer security," *IEEE Internet Things J.*, vol. 12, no. 12, pp. 18 471–18 483, Jun. 2025.

[20] L. Zhang, Y. Wang, H. Chen, and Y. Cao, "Physical-layer security of the NOMA-assisted ISAC systems under near-field scenario," *IEEE Internet Things J.*, vol. 12, no. 12, pp. 18 546–18 553, Jun. 2025.

[21] A. A. Nasir, "Max-min secrecy rate optimization through beam focusing in near-field communications," *IEEE Commun. Lett.*, vol. 28, no. 7, pp. 1594–1598, Jul. 2024.

[22] M. M. R. andand Limei Peng, "DRL-based physical layer security optimization in near-field MIMO systems," *IEEE Internet Things J.*, vol. 12, no. 12, pp. 18 606–18 615, Jun. 2025.

[23] M. Li, L. Fan, A. Cummings, X. Zhang, M. Pan, and Z. Han, "Hybrid quantum classical machine learning with knowledge distillation," in *IEEE Int. Conf. Commun.*, Denver, CO, USA, Jun. 2024, pp. 1139–1144.

[24] C. Ren, Z. Y. Dong, H. Yu, M. Xu, Z. Xiong, and D. Niyato, "ESQFL: Digital twin-driven explainable and secured quantum federated learning for voltage stability assessment in smart grids," *IEEE J. Sel. Topics Signal Process.*, vol. 18, no. 5, pp. 964–978, Jul. 2024.

[25] S. Park, S. B. Son, S. Jung, and J. Kim, "Dynamic quantum federated learning for UAV-based autonomous surveillance," *IEEE Trans. Vehi. Technol.*, vol. 74, no. 5, pp. 8158–8170, May 2025.

[26] S. M, "Machine learning and quantum computing for 5G/6G communication networks - a survey," *Int. J. Intell. Netw.*, vol. 3, pp. 197–203, 2022.

[27] S. Chen, J. Cotler, H.-Y. Huang, and J. Li, "The complexity of NISQ," *Nat. Commun.*, vol. 14, p. 6001, Sep. 2023.

[28] K. Yu, C. Chakraborty, D. Xu, T. Zhang, H. Zhu, O. Alfarraj, and A. Tolba, "Hybrid quantum classical optimization for low-carbon sustainable edge architecture in RIS-assisted AIoT healthcare systems," *IEEE Internet Things J.*, vol. 11, no. 24, pp. 38 987–38 998, Dec. 2024.

[29] P. Zhang, L. Pan, T. Laohapensaeng, and M. Chongcheawchamnan, "Hybrid beamforming based on an unsupervised deep learning network for downlink channels with imperfect CSI," *IEEE Wirel. Commun. Lett.*, vol. 11, no. 7, pp. 1543–1547, Jul. 2022.

[30] Y. Yuan, G. Zheng, K.-K. Wong, B. Ottersten, and Z.-Q. Luo, "Transfer learning and meta learning-based fast downlink beamforming adaptation," *EEE Trans. Wirel. Commun.*, vol. 20, no. 3, pp. 1742–1755, Mar. 2021.

[31] J. Zhang, W. Xia, M. You, G. Zheng, S. Lambotharan, and K.-K. Wong, "Deep learning enabled optimization of downlink beamforming under per-antenna power constraints: Algorithms and experimental demonstration," *EEE Trans. Wirel. Commun.*, vol. 19, no. 6, pp. 3738–3752, Jun. 2020.

[32] M. Qurratulain Khan, A. Gaber, P. Schulz, and G. Fettweis, "Machine learning for millimeter wave and terahertz beam management: A survey and open challenges," *IEEE Access*, vol. 11, pp. 11 880–11 902, Feb. 2023.

[33] J. Zhang, G. Zheng, T. Koike-Akino, K.-K. Wong, and F. A. Burton, "Hybrid quantum-classical neural networks for downlink beamforming optimization," *IEEE Trans. Wireless Commun.*, vol. 23, no. 11, pp. 16 498–16 512, Nov. 2024.

[34] J. Nie, Y. Cui, Z. Yang, W. Yuan, and X. Jing, "Near-field beam training for extremely large-scale MIMO based on deep learning," *IEEE Trans. Mobile Comput.*, vol. 24, no. 1, pp. 352–362, Jan. 2025.

[35] G. J. andand Chenhao Qi, "Near-field beam training based on deep learning for extremely large-scale MIMO," *IEEE Commun. Lett.*, vol. 27, no. 8, pp. 2063–2067, Aug. 2023.

[36] Z. Xu, Z. Wu, and L. Dai, "How to enhance spectrum efficiency for near-field communications: From LDMA to NOMA?" *IEEE Trans. Commun.*, vol. 73, no. 11, pp. 10 709–10 723, Nov. 2025.

[37] I. Batool, M. M. Fouda, M. Ismail, M. I. Ibrahem, Z. Md Fadlullah, and N. Kato, "Quantum-enhanced massive mimo beamforming for 6G IoT networks: A QAOA-based optimization framework," *IEEE Open J. Commun. Soc.*, vol. 7, pp. 222–238, 2026.

[38] N. A. Mitsiou, I. Krikidis, and G. K. Karagiannidis, "Quantum approximate optimization algorithm for MIMO with quantized b-bit beamforming," *IEEE J. Sel. Top. Signal Process.*, vol. 19, no. 6, pp. 1072–1085, Sep. 2025.

[39] M. P. Cuéllar, "What we can do with one qubit in quantum machine learning: ten classical machine learning problems that can be solved with a single qubit," *Quantum Machine Intell.*, vol. 6, no. 2, p. 76, Nov. 2024.

[40] P. Senapati, S. Y.-C. Chen, B. Fang, T. M. Athawale, A. Li, W. Jiang *et al.*, "PQML: Enabling the predictive reproducibility on NISQ machines for quantum ML applications," in *2024 IEEE Int. Conf. Quantum Comput., Eng.*, vol. 01, Montreal, Canada, Sep. 2024, pp. 1413–1424.

[41] H.-Y. Huang, Y. Liu, M. Broughton, I. Kim, A. Anshu, Z. Landau, and J. R. McClean, "Learning shallow quantum circuits," in *Proc. ACM Symp. Theory Comput.*, Vancouver, BC, Canada, Jun. 2024, pp. 1343–1351.

[42] M. Liu, C. Pan, K. Zhi, H. Ren, and J. Wang, "Hybrid precoding design for near-field wideband thz systems with spatial non-stationarity," *IEEE Commun. Lett.*, vol. 28, no. 10, pp. 2372–2376, Oct. 2024.

[43] K. T. Selvan and R. Janaswamy, "Fraunhofer and fresnel distances: Unified derivation for aperture antennas," *IEEE Antennas Propag. Mag.*, vol. 59, no. 4, pp. 12–15, Aug. 2017.

[44] J. Xiao, J. Wang, and Y. Liu, "Channel estimation for pinching-antenna systems (PASS)," *IEEE Commun. Lett.*, vol. 29, no. 8, pp. 1789–1793, Aug. 2025.

[45] D. J. Powell and M. M. Skolnick, "Using genetic algorithms in engineering design optimization with non-linear constraints," in *Proc. 5th Int. Conf. Genetic Algorithms*, San Francisco, CA, USA, 1993, p. 424–431.

[46] E. Zeydan, C. D. Alwis, R. Khan, Y. Turk, A. Aydeger, T. R. Gadekallu *et al.*, "Quantum technologies for beyond 5G and 6G networks: Applications, opportunities, and challenges," *IEEE Open J. Commun. Soc.*, vol. 6, pp. 6383–6420, 2025.

[47] X. Liu, A. Angone, R. Shaydulin, I. Safro, Y. Alexeev, and L. Cincio, "Layer VQE: A variational approach for combinatorial optimization on noisy quantum computers," *IEEE Trans. Quantum Eng.*, vol. 3, pp. 1–20, Jan. 2022.

[48] X. Liu, G. Liu, H.-K. Zhang, J. Huang, and X. Wang, "Mitigating barren plateaus of variational quantum eigensolvers," *IEEE Trans. Quantum Eng.*, vol. 5, pp. 1–19, Mar. 2024.

[49] D. Wierichs, J. Izaac, C. Wang, and C. Y.-Y. Lin, "General parameter-shift rules for quantum gradients," *Quantum*, vol. 6, p. 677, Mar. 2022.

[50] N. T. Nguyen, L. V. Nguyen, N. Shlezinger, A. L. Swindlehurst, and M. Juntti, "Fast deep unfolded hybrid beamforming in multiuser large MIMO systems," in *Proc. Asilomar Conf. Sig., Sys., Comput.*, Pacific Grove, CA, USA, Oct. 2023, pp. 486–490.

[51] A. Saad, A. P. Engelbrecht, and S. A. Khan, "An analysis of differential evolution population size," *Applied Sciences*, vol. 14, no. 21, p. 9976, Oct. 2024.

[52] R. Storn and K. Price, "Differential evolution – a simple and efficient heuristic for global optimization over continuous spaces," *J. Glob. Optim.*, vol. 11, no. 4, pp. 341–359, Dec. 1997.

[53] S. Das, Suganthan, and P. Nagaratnam, "Differential evolution: A survey of the state-of-the-art," *IEEE Trans. Evol. Comput.*, vol. 15, no. 1, pp. 4–31, Feb. 2011.

[54] B.-C. Wang, H.-X. Li, J.-P. Li, and Y. Wang, "Composite differential evolution for constrained evolutionary optimization," *IEEE Trans. Syst. Man. Cybern.*, vol. 49, no. 7, pp. 1482–1495, Jul. 2019.

[55] T. Runarsson and X. Yao, "Stochastic ranking for constrained evolutionary optimization," *IEEE Trans. Evol. Comput.*, vol. 4, no. 3, pp. 284–294, Sep. 2000.

[56] J. Nocedal and S. J. Wright, *Numerical Optimization*, 2nd ed., ser. Springer Series in Operations Research and Financial Engineering. New York: Springer, 2006.

[57] M. Merrouchi, K. Atifi, M. Skittou, Y. Benyoussef, and T. Gadi, "Autolropt: An efficient optimizer using automatic setting of learning rate for deep neural networks," *IEEE Access*, vol. 12, pp. 83 154–83 168, Jun. 2024.

[58] J. Chen, Q. Chen, J. Jia, B. Yin, and X. Wang, "Passive sensing in a near-field multi-ISAC system with imperfect CSI," *IEEE Trans. Cognit. Commun. Netw.*, vol. 12, pp. 4186–4197, 2026.

[59] S. Shakoor, N.-S. Vo, Q. Nhat Le, B. Canberk, C.-K. Wen, H. Shin, and T. Q. Duong, "Weighted sum rate maximization for RIS-mounted UAV-aided cell-free ISAC systems," *IEEE Trans. Commun.*, vol. 74, pp. 4278–4290, Jan. 2026.

[60] G. Buonaiuto, F. Gargiulo, G. D. Pietro, M. Esposito, and M. Pota, "The effects of quantum hardware properties on the performances of variational quantum learning algorithms," *Quantum Machine Intelligence*, vol. 6, p. 9, Feb. 2024.